Downloaded from orbit.dtu.dk on: Apr 16, 2024

DTU Library

# Life time evolution of coronal holes

Jerčić, Veronika; Heinemann, Stephan G.; Temmer, Manuela; Dumbović, Mateja; Vennerstrøm, Susanne; Verbanac, Giuliana; Hofmeister, Stefan J.; Veronig, Astrid M.

*Published in:*
Solar Physics

*Publication date:*
2024

*Document Version*
Early version, also known as pre-print

Link back to DTU Orbit

*Citation (APA):*
Jerčić, V., Heinemann, S. G., Temmer, M., Dumbović, M., Vennerstrøm, S., Verbanac, G., Hofmeister, S. J., & Veronig, A. M. (2024). Life time evolution of coronal holes. Manuscript submitted for publication.

**General rights**
Copyright and moral rights for the publications made accessible in the public portal are retained by the authors and/or other copyright owners and it is a condition of accessing publications that users recognise and abide by the legal requirements associated with these rights.

- Users may download and print one copy of any publication from the public portal for the purpose of private study or research.
- You may not further distribute the material or use it for any profit-making activity or commercial gain
- You may freely distribute the URL identifying the publication in the public portal

If you believe that this document breaches copyright please contact us providing details, and we will remove access to the work immediately and investigate your claim.

Solar Physics
DOI: 10.1007/•••••-•••-•••-••••-•

# Life time evolution of coronal holes

*Solar Physics*

**Veronika Jerčić[1,2] · Stephan G. Heinemann[1] · Manuela Temmer[1] · Mateja Dumbović[1,3] · Susanne Vennerstroem[4] · Giuliana Verbanac[2] · Stefan J. Hofmeister[1] · Astrid M. Veronig[1]**

© Springer ••••

**Abstract** We investigate the evolution of eight well-observed persistent coronal holes (CHs) with life spans of 5–12 solar rotations, that were observed between 2010 and 2015. The aim is to increase our understanding of the evolution of CHs, as well as to investigate the basic physical mechanisms that govern the CH behaviour over its lifetime. Using combined AIA/SDO and HMI/SDO data, we derive several CH parameters such as area, intensity, and magnetic field characteristics as function of time. Using in-situ data from the ACE satellite located at L1, we study the corresponding solar wind plasma measurements. We find that 6 out of 8 CHs in our data set reveal a steady increase in the area followed by a decrease. For those we derive the average absolute change of area between two points in the growing phase with $(10.2 \pm 3.5) \cdot 10^8$ km$^2$ per day, while for the decaying phase it is $(8.6 \pm 3.7) \cdot 10^8$ km$^2$ per day. We further found that the CH magnetic field strength is strongly related to the amount of area strong flux tubes contribute to the CH area. However, there is no correlation between the magnetic field and the total CH area itself, hence, the magnetic

✉ V. Jerčić
veronika.jercic@gmail.com

✉ S.G. Heinemann
stephan.heinemann@hmail.at

✉ M. Temmer
manuela.temmer@uni-graz.at

[1] University of Graz, Institute of Physics, Universitätsplatz 5, 8010 Graz, Austria

[2] University of Zagreb, Faculty of Science, Department of Geophysics, Croatia

[3] University of Zagreb, Faculty of Geodesy, Hvar Observatory, Croatia

[4] National Space Institute, DTU Space, Denmark

arXiv:1907.02795v2 [astro-ph.SR] 16 Jul 2019

field variation follows a different evolutionary pattern. With the in-situ proton bulk speed, we derive for the growing area phase a strong correlation (Pearson $cc = 0.69$) and for the decaying phase a moderate one ($cc = 0.45$).

**Keywords:** ??

## 1. Introduction

Coronal holes (CH) are relatively stable, long-lived structures on the Sun most easily identified in the solar corona observed in extreme ultra violet (EUV) or soft X-ray images, where they appear as regions of strongly reduced emission. CHs are characterized by an open magnetic field configuration along which ionized atoms and electrons can freely escape into interplanetary space, forming high speed solar wind streams (HSS, Krieger, Timothy, and Roelof, 1973; Nolte *et al.*, 1976; Cranmer, 2002). The interaction of HSSs with the ambient slow solar wind forms stream interaction regions (SIRs) which can develop into co-rotating interaction regions (CIRs, Wilcox, 1968; Tsurutani *et al.*, 2006) if the CH persists over multiple rotations. Persistent CIRs are usually observed from in-situ data in every consecutive solar rotation while the source CH exists. Similar to interplanetary coronal mass ejections (ICMEs), CIR structures can cause geomagnetic effects but on average on a less intense level since their total energy input to the Earth's magnetosphere is usually lower (Verbanac *et al.*, 2011; Verbanac *et al.*, 2013). However, due to the recurrent nature of CIRs, their impact on the Earth's magnetosphere is more important than the one caused by ICMEs (Vršnak, Temmer, and Veronig, 2007; Tsurutani *et al.*, 2006) especially during times of low solar activity. Thus, for the purpose of geoeffectiveness, the evolution of recurrent CHs needs to be comprehensively understood.

In X-ray and EUV, CHs appear as dark structures on the Sun as they radiate less than the surrounding corona due to their decreased plasma density caused by the out-flowing solar wind plasma. CHs are observed in many different sizes and shapes, and can be found at all latitudes on the Sun, from equatorial regions up to the poles (Krieger, Timothy, and Roelof, 1973; Harvey and Sheeley, 1978). Their appearance depends on the phase of the solar cycle and with that on the global magnetic field structure (Mikhailutsa, 1995; Ikhsanov and Tavastsherna, 2015; Bilenko and Tavastsherna, 2016). Ikhsanov and Tavastsherna (2015) showed that there are two magnetic field systems that play a main role in the evolution of the solar magnetic cycle and whose effects can be seen in the appearance of CHs. At high-latitudes, the large scale magnetic field system shows itself as extended polar CHs. At low-latitudes, the small scale magnetic system manifests itself as localized CHs that are the result of decaying local sunspot groups or generated by other mechanisms that enable to "open" the magnetic field, such as CME/filament eruptions, flux accumulation, or flux emergence (e.g., Webb *et al.*, 1978; Heinemann *et al.*, 2018a).

Most studies focus on a snap-shot of the CH during its lifetime, and there is less focus on the evolutionary aspects. It is known that the area and the mean magnetic field strength of a CH are dependent on its age (Bohlin, 1977

and Bohlin and Sheeley, 1978). Further, by Heinemann *et al.* (2018a,b) the evolution of one particular CH from 2012 is analyzed using combined SDO and STEREO data. They identified a 3-phase evolution of the CH under study, with a growing, maximum and a decaying phase. They found that the evolution of a CH manifests different behaviour in different phases. The three phases can be seen in EUV intensity but also in the associated HSS measured at 1AU. According to their analysis the CH parameters seem to be more stable while the CH forms and up to its maximum compared to the decaying processes. As for the magnetic properties of a CH, they concluded that they are governed by a small scale-structures of unipolar magnetic field, called flux tubes (FTs).

Here, we expand this case study by analyzing in detail the morphology and magnetic field characteristics of a set of eight long-lived CHs to obtain more general insight into their evolutionary processes. Besides investigating the on-disk CH parameters, we also analyze the in-situ signatures of the corresponding HSSs observed near Earth (L1 point).

## 2. Methods and Data

### 2.1. Data

We investigated the Solar Dynamics Observatory (SDO; Pesnell, Thompson, and Chamberlin, 2012) era, operative since mid of 2010, in search of long-lived CH structures. As CHs are best visible as dark regions in the Atmospheric Imaging Assembly (AIA; Lemen *et al.*, 2012) 193Å channel revealing emission from Fe XII ions at a peak response temperature of $1.6 \cdot 10^6$ K, we inspected full-disk AIA 193Å images at a high spatial resolution of 1.5-arcsec at a plate scale of 0.6 arcsec/pixel (Lemen *et al.*, 2012). In the period from September 2010 until November 2015, we identified in total eight recurrent CHs that were observed over 5–12 months. For those we studied the magnetic properties using 720s line-of-sight (LoS) magnetograms from the Helioseismic and Magnetic Imager (HMI; Schou *et al.*, 2012; Couvidat *et al.*, 2016) on board SDO. HMI continuously observes the full solar disk at 6173Å with a spatial resolution of 1 arcsec at a plate scale of 0.505 arcsec/pixel. To associate CHs to in-situ measured recurrent HSSs and to study their solar wind bulk velocity near Earth we used data from the Solar Wind Electron, Proton, and Alpha Monitor (SWEPAM; McComas *et al.*, 1998, 1 hour averages) provided by NASA's Advanced Composition Explorer (ACE; Stone *et al.*, 1998) satellite.

### 2.2. CH segmentation

The CH boundaries were extracted from EUV 193Å filtergrams using the Collection of Analysis Tools for Coronal Holes (CATCH; Heinemann *et al.*, 2019), i.e. an enhanced intensity thresholding method using a gradient modulation at the CH boundary. Figure 1 shows an example of the evolution of a CH (CH6, see Table 1) as seen in EUV image data where the red line marks the boundary of the CH as extracted using CATCH. By co-registering the previously

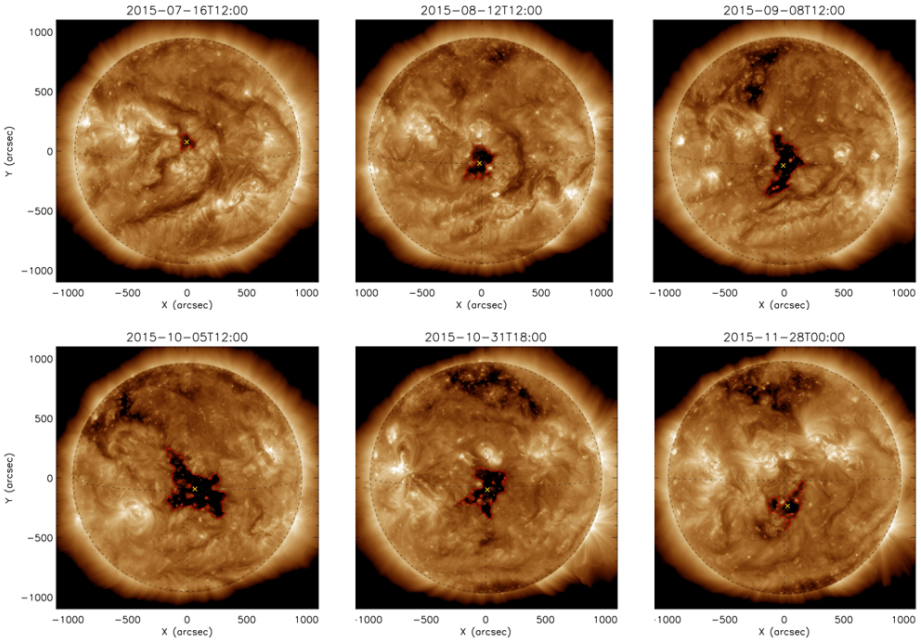


**Figure 1.** Example of the evolution of a CH (CH6, see Table 1) in EUV 193Å filtergrams. The red line marks the boundary of the CH extracted with CATCH and the yellow cross marks the position of the center of mass.

extracted boundary from EUV images onto HMI magnetograms, we derived the CH magnetic properties.

Within the derived boundaries, the following CH properties were extracted from EUV filtergrams: area, mean and median intensity, position of the center of mass (CoM), and the latitudinal and longitudinal extent. And from HMI magnetograms, the following magnetic properties were derived: signed and unsigned mean magnetic field strength ($B_{s/us}$), signed and unsigned magnetic flux ($\Phi_{s/us}$), flux balance ($\Phi_B$; ratio of signed to unsigned magnetic flux), number of weak and strong FTs ($N_{FT,strong/weak}$) which constitute the fine structure of a CH and are defined above a threshold value of ±20 G (Heinemann *et al.*, 2018b), flux ratio of weak and strong FTs ($r_{A,strong/weak}$; proportion of open flux from FTs to the CH open flux) and area ratio of weak and strong FTs ($r_{\Phi,strong/weak}$; ratio of the area from FTs to the CH area). The calculations were performed using CATCH, for more details we refer to Heinemann *et al.* (2019).

### 2.3. Solar wind

For each CH we searched for typical signatures of SIRs and HSSs in the in-situ data. We followed the criteria as described by Jian *et al.* (2006), such as the total perpendicular pressure should reach a maximum while the solar wind speed increases steadily. Additional criteria were the compression of particle density and magnetic field at the interface, as well as flow deflection and temperature

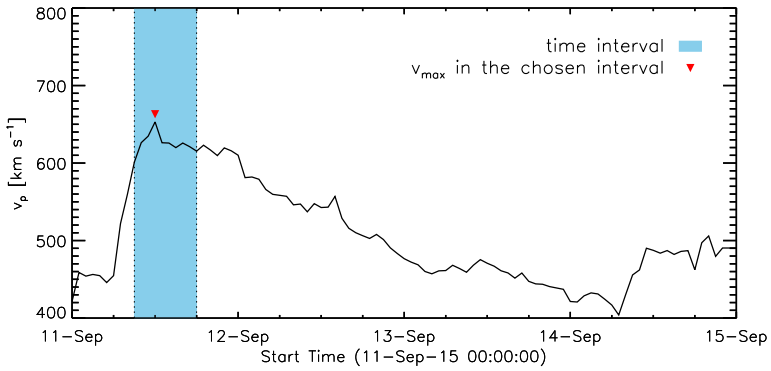


**Figure 2.** An example of the in-situ speed profile and extraction of the maximum solar wind bulk speed using the average over a time window (−3 and +6 hours; marked as the blue shaded area) around the peak. The red triangle marks the peak of the HSS in the chosen time interval.

increase. To appropriately match HSSs to the identified CHs a time interval is used to investigate the in-situ measured profile. The time interval spans 10 days starting from the date of the CH's central meridian passage. Within this 10 day time window, we manually identified the HSS, derived its peak in proton bulk velocity and cross-checked with ready HSS lists (maintained by S. Vennerstroem for 2010–2014 and S. Hofmeister for 2015). Upon verification, the maximum speed of the HSS was derived by averaging the proton bulk velocity over 3 hours before and 6 hours after the identified peak (see Fig. 2).

## 3. Results

We observed a steady change in the area in 6 out of 8 CHs in our data set, that is characterized by a distinctly visible growing and a decaying phase. In the following, we refer to it as a regular change in area. The remaining 2 CHs show a much more variable change in area due to influences from the surroundings. We consider them as outliers, and refer to their change as an irregular change in the CH area. The 2 CHs with an irregular change are not included in the quantitative analysis of magnetic and solar wind properties, nor in any of the correlations calculated.

### 3.1. Area and intensity

As an example of the regular change in area, we describe CH1 (Fig. 3), showing a small local maximum in the early evolution followed by a general growth leading to a maximum in area of $7.3 \cdot 10^{10}$ km$^2$. For all CHs under study we derive area maxima in the range of 4.1 to $24.5 \cdot 10^{10}$ km$^2$ (see Tab. 1). After reaching the maximum, a decrease in area is revealed and the CH is tracked until it can no longer be observed. As described the growth phase is characterized by an increase in the CH area. In the following, when referring to a growth phase we

imply that the maximum point is also included as part of it. In some cases of the growing phase small variations are observed, but in general, a growing trend is present. The average absolute change of area between two points in the growing phase of the regular CHs is $(10.2 \pm 3.5) \cdot 10^8$ km$^2$ per day. The average absolute change in the decaying phase is $(8.6 \pm 3.7) \cdot 10^8$ km$^2$ per day.

CH7 and CH8 (see Tab. 1) are outliers to the described regular area evolution. CH7 shows two peaks in the area evolution. One at the beginning, while the other close to the end of the CH's lifetime, with the two peaks of comparable values, 4.1 and $3.6 \cdot 10^{10}$ km$^2$, so it's not possible to define a growing and a decaying phase. CH8, on the other hand, shows an almost constant value of area during its evolution. It is related to the southern polar CH from which it extends in the first solar rotation, then detaches from it just to attach again during the last two solar rotations (Fig. 3).

Figure 3 shows the time-lines of area and intensity for all 8 CHs we studied. Analyzing the relation between intensity and area profiles, we find an anti-correlation between these properties independent on the way the CHs evolve.

### 3.2. Magnetic properties

#### *3.2.1. Magnetic field strength and flux*

The main driver of a CH's evolution seems to be the underlying magnetic field (Hofmeister *et al.*, 2017; Heinemann *et al.*, 2018b) and in order to understand CHs and how they evolve we need to derive their magnetic field characteristics. Since they are defined as regions of open flux, the flux balance (measure of open flux) indicates that we have open flux in the analyzed structures (see Appendix, Fig. 10). Figure 4 shows the evolution of signed (red) and unsigned (blue) mean magnetic field strength together with the area evolution (dotted black line). For an easier visual analysis we present absolute values of the mean signed magnetic field strength. Inspecting the magnetic field strength of the regular CH1 it shows a growing trend together with the area, resulting in a local maximum (8.1 G and 3.9 G for the unsigned and the absolute value of signed magnetic field strength, respectively), one rotation before the area peaks. Opposed to the steadily shrinking area of CH1, the magnetic field shows only a small decrease and then a growth again. In the last rotation revealing a sudden and fast decrease in the area (from 5.5 to $1.4 \cdot 10^{10}$km$^2$), the maximum magnetic field is reached (9.2 G and 6.0 G, the unsigned and the absolute value of signed magnetic field strength, respectively). Considering the regular CHs in our data set (Fig. 4), we conclude that the evolution of signed and unsigned mean magnetic field strength is, in general, not related to the evolution of the CH area. Additionally, if we would include the two CHs with an irregular change in area into this analysis the conclusion wouldn't change.

Comparing the magnetic field parameters for CH1–CH6, we find that the mean signed and unsigned magnetic field strengths are correlated, with a Pearson correlation coefficient of 0.83 with a 95% CI of [0.73, 0.92]. Further, comparing the change of signed and unsigned magnetic flux (see Appendix, Fig. 11) with the change of the CH area we obtain an expected strong correlation. It is expected

**Table 1.**: List of CHs under study with their minimum and maximum mean intensity and area. As well, mean latitude in HEEQ of their center of mass (CoM) and the sign of each CH. If it is a regular CH the type is marked with R if it is an outlier it is marked with O.

| CH | Time range | Type | Min-Max $\bar{I}$ [DN] | Min-Max $\bar{A}_{CH}$ [$10^{10}$ km$^2$] | Mean latitude of CoM [°] | Polarity | Average growth rate [$10^8$ km$^2$/day] | Average decay rate [$10^8$ km$^2$/day] |
|---|---|---|---|---|---|---|---|---|
| 1 | 02-11–10-11 | R | 22-56 | 0.7-7.0 | $-7 \pm 13$ | − | 4.7 | −8.3 |
| 2 | 02-12–10-12 | R | 21-38 | 1.4-8.6 | $6 \pm 7$ | − | 5.6 | −6.3 |
| 3 | 01-13–11-13 | R | 25-42 | 0.8-13.3 | $18 \pm 15$ | − | 8.3 | −9.6 |
| 4 | 04-13–01-14 | R | 24-69 | 0.8-8.1 | $4 \pm 4$ | + | 15.8 | −3.6 |
| 5 | 08-13–02-14 | R | 29-57 | 1.8-18.6 | $32 \pm 7$ | + | 17.4 | −15.0 |
| 6 | 06-15–11-15 | R | 19-32 | 0.7-7.7 | $-1 \pm 6$ | + | 10.0 | −11.3 |
| 7 | 09-10–02-11 | O | 17-45 | 0.7-4.1 | $17 \pm 5$ | − | | |
| 8 | 04-15–09-15[1] | O | 21-30 | 2.6-24.5 | $-38 \pm 13$ | − | | |

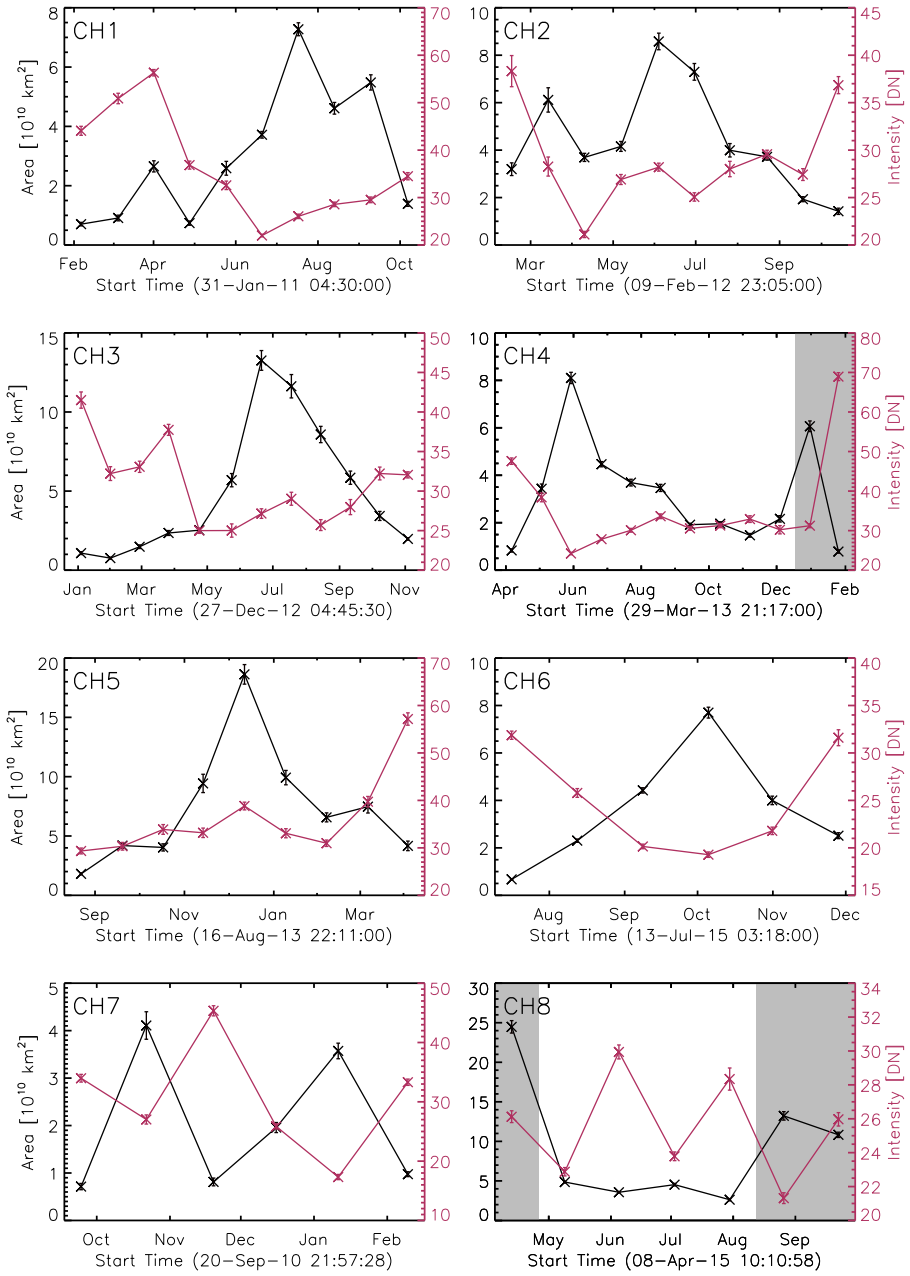


**Figure 3.** Evolution of area (black) and intensity (red) for all CHs under study, CH1–CH6 (regular) and CH7–CH8 (irregular, see Tab. 1). The shaded area for CH4 marks the evolution of area influenced by the filament eruption. The shaded areas for CH8 mark the solar rotations when the observed CH was attached to the polar CH.

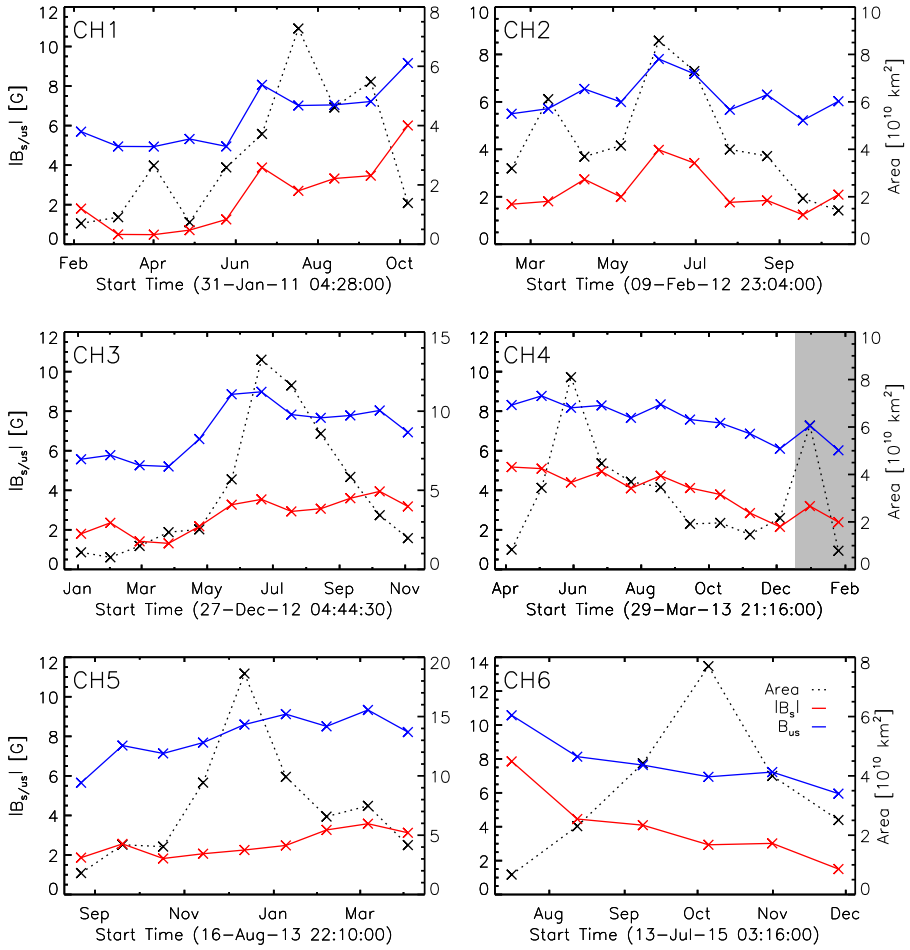


**Figure 4.** Evolution of signed (red) and unsigned (blue) mean magnetic field strength with CH area (dotted black) for CH1–CH6. Absolute values of signed mean magnetic field are plotted for easier visual representation. The shaded area for CH4 marks the evolution of area influenced by the filament eruption.

because of the magnetic flux definition followed by the fact that the CH area usually changes more than the CH magnetic field strength. In that sense, the magnetic flux also shows the same pattern of evolution as the area. The average absolute change of signed flux in the growing phase per day is $(3.2\pm1.6)\cdot10^{19}$Mx, while the average absolute change of signed flux in the decaying phase per day is $(2.8 \pm 0.7) \cdot 10^{19}$Mx.

### *3.2.2. Magnetic fine structure: Flux Tubes*

As the primary source of flux of the dominant polarity of a CH, we investigate the role of the magnetic fine structure in the form of FTs during the evolution of

CHs. We separate strong FTs with a mean magnetic field strength higher than 50 G and weak FTs with a magnetic field strength between 20 and 50 G (cf. Heinemann *et al.*, 2018b). The number of strong FTs within a CH lies in the range from 7 to 215 with an average of $17 \pm 6$ per $10^{10}$ km$^2$. Weak FTs are more numerous and span a larger range, from 82 to 3282 FTs in a certain CH with an average of $130 \pm 20$ per $10^{10}$ km$^2$. In the Figure 5 we can very distinctly notice that during the entire evolution strong FTs (blue) have a higher contribution to the total signed flux of the CH compared to the weak ones (red). For the flux we derive a contribution between a maximum of about 70% and a minimum of about 32% to the total signed flux of a CH. We can notice from Figure 5 that the time-lines of strong and weak FTs flux ratio look like mirror images of each other. As the contribution of one type of FTs decreases the contribution of the other increases (and vice versa). The maximum difference between strong and weak FTs flux ratio is in general smaller for CH1, CH3 and CH5 than for CH2, CH4, and CH6. We hardly notice a particular pattern that could connect to the CH area evolution. Flux ratio, similar to the mean magnetic field strength, shows a more unpredictable change, not corresponding to the CH area evolution.

### 3.3. Solar wind properties

The in-situ measured solar wind bulk peak speed, related to the CHs under study, ranges from 330 km s$^{-1}$ to 820 km s$^{-1}$. To isolate the outflow from a single CH under study, we excluded for the in-situ comparison data points marked with a red square in Figure 6. Those data points were defined for cases when a CH, during its evolution was observed to be close to another CH or related to closely surrounding dark patchy structures (candidates of open flux that may contribute to the total measured solar wind plasma bulk velocity). The CME time intervals according to Richardson and Cane (2010) list were excluded from the calculations of the average HSS peak speed. The HSS evolution is shown in Figure 6 for CH1–CH6. For most cases a weak HSS is already observed at the beginning of the CH formation and close to its end. Only for CH5 we did not observe a HSS in the last solar rotation, while for CH6 we did not observe a related HSS in the first solar rotation. As can be seen from the same figure, for the major part of the evolution, the HSS velocities follow the changes in the CH area. Certain deviations (excluded data points) are noticeable on the figure, and as mentioned before, are mostly caused by additional (open) structures, visible in EUV images.

## 4. Correlations

We can see already from Figure 5, and we know from previous research (Hofmeister *et al.*, 2017; Heinemann *et al.*, 2018b; Heinemann *et al.*, 2019; Hofmeister *et al.*, 2019) how important strong FTs are in defining the magnetic properties of a CH. Here we investigate the differences or similarities between different stages of the CH lifetime. We plot, separately for growing and decaying phase, some already known to be strong correlations between FTs number, CH area,

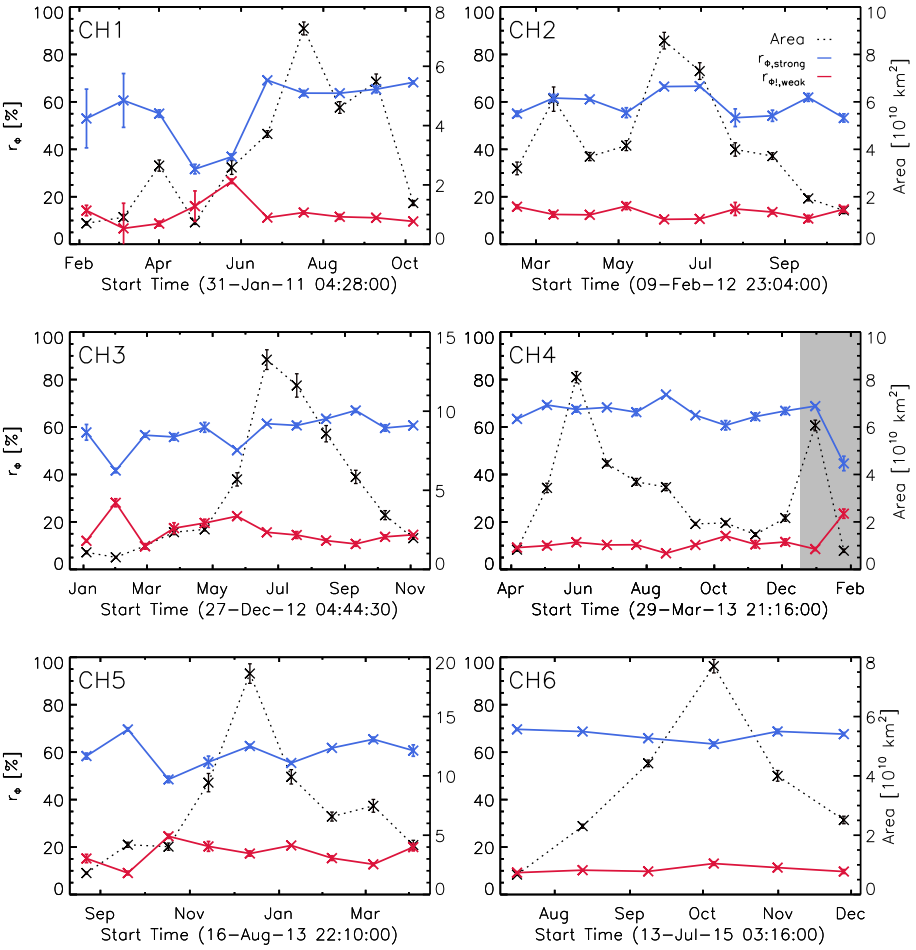


**Figure 5.** Evolution of weak (red) and strong (blue) FTs flux ratio for CH1–CH6 with the evolution of area (dotted black). The shaded area for CH4 marks the part of the evolution influenced by the filament eruption.

FTs area ratio and the absolute value of the signed mean magnetic field strength (Fig. 7). The number of FTs, both strong and weak, show a very high correlation with the area of a CH (Pearson cc=0.97 with a 95% CI of [0.93, 0.98] and cc=0.92 with a 95% CI of [0.88, 0.95] for weak and strong FTs respectively). No significant differences are found between the two evolutionary phases and the data points are observed to be evenly scattered in both phases of a CH's evolution. The correlation coefficients for each phase can be found in the Appendix (see Tab. 2).

The mean magnetic field strength depends substantially on the strong FTs and the percentage area they cover. The correlation between the strong FTs area ratio and the absolute value of the signed mean magnetic field strength has a Pearson correlation coefficient of 0.99 and a 95% CI of [0.98, 0.99]. A fit reveals a near 1-to-1 correlation with $|B_s| = 1.1 \cdot r_{A,strong}$. Looking at the right panels of

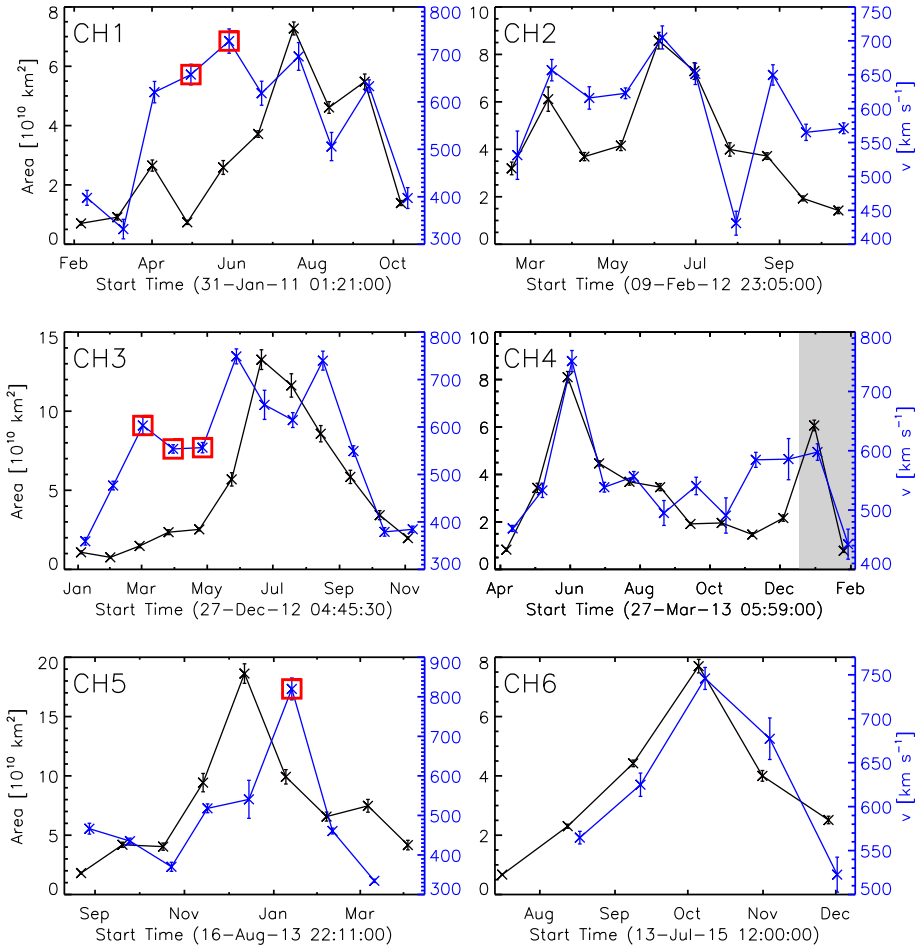


**Figure 6.** Evolution of CH1–CH6 corresponding HSSs measured near Earth (blue) and area (black). The shaded area for CH4 marks the part of the evolution influenced by the filament eruption. For the last solar rotation of CH5 we do not observe a HSS, while for CH6 no HSS is detected in the first solar rotation. Red squares mark the outliers (see text) excluded from calculations.

Figure 7, there are no distinct differences between the correlation in the growing and decaying phase. Again, the data points are evenly scattered and contribute equally to the strong correlation we observe. The correlation coefficients for each phase can be found in the Appendix (see Tab. 2).

Figure 8 shows a scatter plot of the absolute value of the mean signed magnetic field strength and CH area. We find no correlation between the parameters. For small CHs (areas less than $3 \cdot 10^{10}$ km$^2$) the signed mean magnetic field strength covers a broad range of values, from 0.5 up to 7.9 G. For big CHs the range of values for the magnetic field strength becomes considerably smaller. For CHs

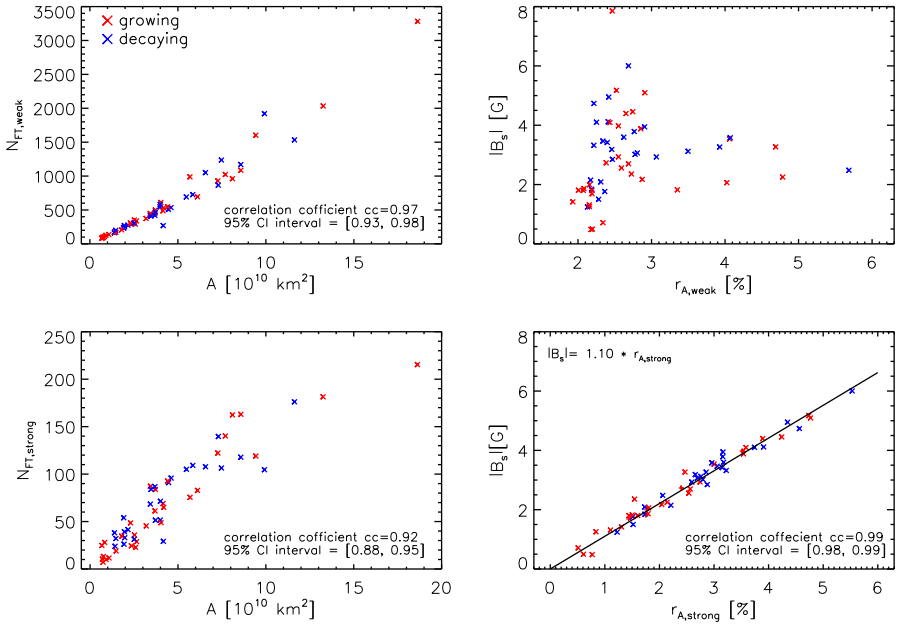


**Figure 7.** Left panels show scatter plots of the number of FTs (weak FTs - top; strong FTs - bottom) and area of a CH. Right panels show scatter plots of FTs area ratio (weak FTs - top; strong FTs - bottom) and the absolute value of the signed mean magnetic field strength of the CH. Data points are divided between the growing (red) and decaying (blue) part of CH's lifetime. The black line represents the linear fit to the data.

with an area bigger than $8 \cdot 10^{10}$ km$^2$ the magnetic field strength values span a range of 2.1 to 4.4 G.

Figure 9 shows the derived HSS peak speed plotted against the CH area. The weak Pearson correlation coefficient of $cc = 0.26$ (95% CI [-0.11, 0.60]) of the

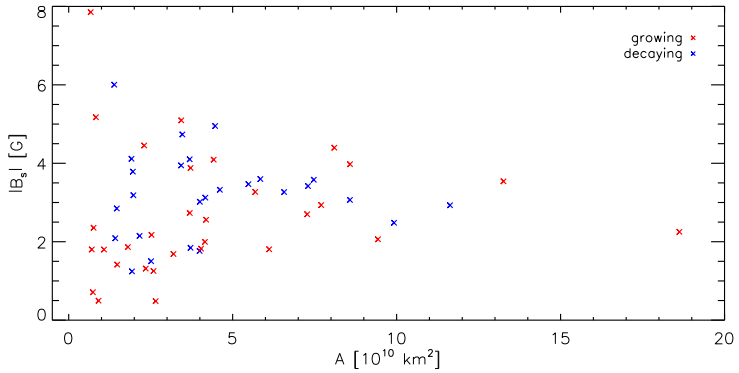


**Figure 8.** Absolute value of signed mean magnetic field strength of CH1–CH6 plotted over CH area with data points divided between the growing (red) and decaying (blue) phase.

properties of all 6 regular CHs reveals that there is no correlation (see upper panel of Fig. 9). We note that when inspecting the correlation coefficients for each of the regular CHs (CH1–CH6) individually, all of them are found to be in the range from 0.45 up to 0.86 (see bottom panel of Fig. 9). Hence, we conclude that the area-speed relation exists but it considerably impairs averaging over the six CHs in our data set. In addition to the linear fit, we give two reference lines from previous studies by Nolte *et al.* (1976) and by Tokumaru *et al.* (2017). We can see that our fit is in between these two reference lines. Most likely due to the diverse data set regarding the CH latitudinal position (see Tab. 1). Due to the changes of the relative position of the measuring satellite in the HSS with the solar latitude of the CH (co-latitude), we get lower HSS velocities for CH located at higher latitudes. To check the dependence of the measured solar wind speed on the co-latitude of the corresponding CH we use the empirical relation from Hofmeister *et al.* (2018) and calculate the effective area ($A_{eff}$) as:

$$A_{eff} = A(1 - \frac{|\varphi_{co}|}{61.4}) \tag{1}$$

where $A$ is the CH area and $\varphi_{co}$ is the co-latitude in degrees. The result is given in the middle panel of Fig. 9 showing the relation of in-situ measured solar wind speed with the effective value of the CH area. In comparison to the non-effective CH area, we notice an increased correlation with less spread of the data points. We also investigate the area-speed correlation separately for the growing (red) and decaying (blue) phase of the CH regular group and give their linear fits (with dashed lines representing the upper and lower error boundaries of the fits, middle panel of Fig. 9). The Pearson correlation coefficient between the HSS velocity and the effective CH area shows a strong correlation in the growing ($cc = 0.69$, 95% CI [0.41, 0.89]) and a moderate one ($cc = 0.45$, 95% CI [0.14, 0.68]) in the decaying phase.

## 5. Outliers

The remaining two CHs not included in the quantitative analysis are considered as outliers to the regular change of area seen in the first six. CH7 has two very distinct peaks in the area evolution. The first decrease in area, between the second and third data point (Fig. 3) was caused by a filament eruption in the vicinity of the CH on the October 30, 2010 at 17:37 UTC (as observed from STEREO A). As a consequence the CH area strongly decreases followed by an increase to its previous size. We note that CH4, which we categorized as regular, shows a sudden increase in area due to a filament eruption on December 4, 2011 at 22:37 UTC. For that reason we excluded the last two data points of CH4 from the quantitative analysis. CH8 is also regarded as a clear outlier, due to its connection with the polar CH in the south. The CH starts as an extension of the polar CH from which it detaches already after the first solar rotation. Considering its rigid rotation the CH doesn't change significantly in its size, however, due to its high latitudinal position, all properties extracted from it, especially the ones regarding magnetic properties have very high uncertainties.

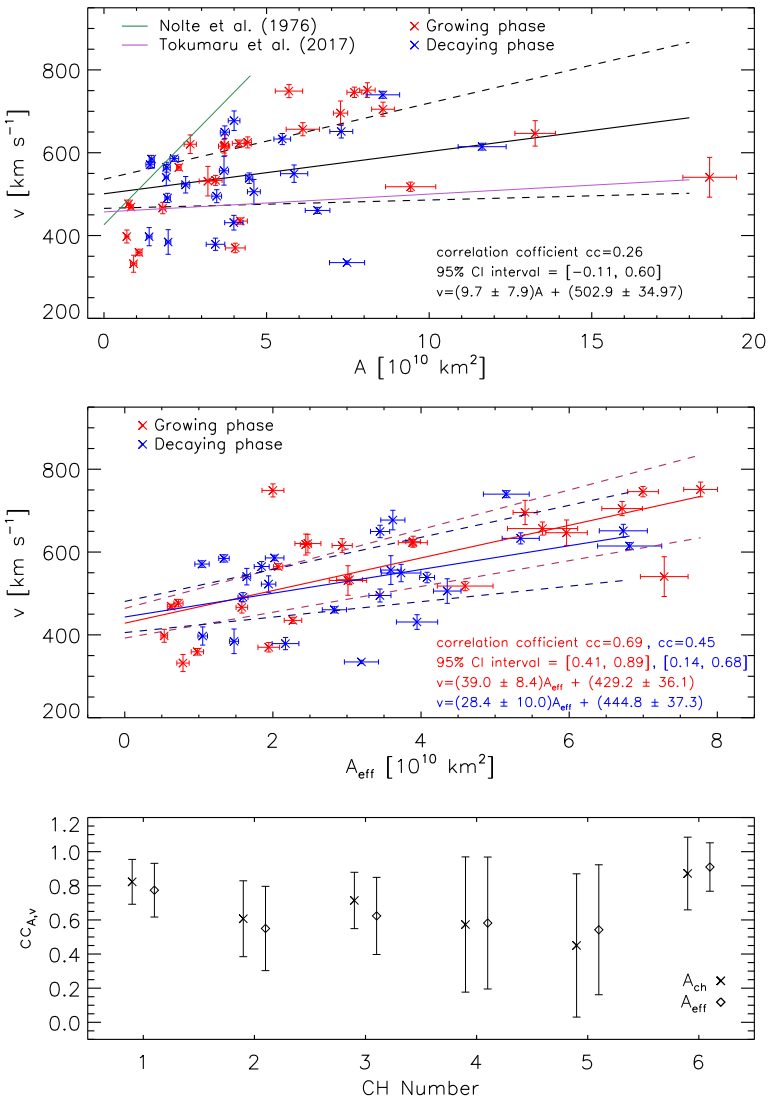


**Figure 9.** Top: HSS peak velocity plotted against CH area. We give the linear fit (black solid line) and its upper and lower error boundaries (dashed lines). Green and purple lines represent two reference fits, taken from Nolte *et al.* (1976) and Tokumaru *et al.* (2017) respectively. Growing (red) and decaying (blue) phases of the CH evolution are marked in different colors. Middle: HSS peak velocity plotted against CH area corrected for in-situ s/c co-latitude. The two colored solid lines represent linear fits for each phase and the dashed lines are the corresponding upper and lower error boundary. Bottom: Comparison of correlation coefficients for the area-speed relation ($cc_{A,v}$) for each CH (CH1–CH6) individually. Calculated for the total CH area and for the effective CH area (see Eq. 1).

## 6. Discussion

In the present study we have investigated the evolution of eight long lived CHs that were visible in the period 2010–2015 covering the rise and maximum of solar cycle 24. As CHs are structures of open field, well observed in the corona, and rooted in the photosphere, the presented analysis aims to study the changes of properties of CHs extracted from AIA/SDO EUV filtergrams and HMI/SDO magnetograms.

### 6.1. Area and intensity

Based on the resulting CH area evolution, 6 out of the 8 CHs under study reveal a growing, (maximum) and decaying phase. The remaining two CHs in our data set were classified as outliers because they do not show a well defined evolutionary pattern in the area. They were clearly influenced by surrounding conditions (filament eruptions, connection to a polar CH). For all 8 CHs we found an anti-correlation between CH area and intensity profile, that has also been found by other authors (e.g. Rotter *et al.*, 2012; Hiremath and Hegde, 2013; Andreeva *et al.*, 2018). Hofmeister *et al.* (2017) showed that the intensity of the inner part of a CH is constant and varies mostly near the boundary. How strong this variations are, depends on the individual CH. The anti-correlation is more pronounced for smaller CHs. Therefore, the observed intensity variations can be well explained by boundary effects and geometry characteristics of the CHs in our data set. Our statistics on 6 regular CHs confirm the already suspected steady change in the CH area (Heinemann *et al.*, 2018a). The values of the average growth and decay rates are consistent with other studies (e.g., Bohlin, 1977). The growth rate falls within the error limit of the value from Bohlin (1977), while the decay rate is somewhat lower. If CHs in general undergo steady changes following a growth and decay phase, would mean a step forward in better understanding and modeling CHs and with that improving space weather forecasts (cf. Temmer, Hinterreiter, and Reiss, 2018).

### 6.2. Magnetic properties

Taking a closer look at how the magnetic field varies over time, we concluded that each CH is its own special case. This goes along with the two case studies of two different CHs and their magnetic properties undertaken by Heinemann *et al.* (2018b) and Andreeva *et al.* (2018). Heinemann *et al.* (2018b) showed that the CH area and the mean magnetic field strength are in a strong correlation, while Andreeva *et al.* (2018) showed that the two occurred in antiphase. According to our 6 regular CHs the relation of the CH area and the magnetic field strength shows that, not only that the magnetic field strength is not correlated with the CH area, but also does it not show any special characteristics in different phases of the CH evolution. Both the signed and unsigned magnetic field strength exhibit similar behaviour. The correlation we found between the magnetic flux and the CH area was expected, because the magnetic field does not change as much as the area does. The rate at which the flux grows in the growing phase and later the rate at which it decays are of comparable values.

Another important parameter is the FTs flux ratio. Similarly as for the magnetic field strength, changes of the flux ratio over time are not related to the CH area evolution. How much the strong FTs contribute to the total signed flux of the CH does not depend on the phase of the evolution itself. The contribution coming from strong FTs is always the dominant in comparison to the contribution of the weak ones, which has already been shown by previous works (Hofmeister *et al.*, 2017; Heinemann *et al.*, 2018b; Hofmeister *et al.*, 2019). That conclusion stays valid at any point of a CHs evolution.

The magnetic field strength is dominantly governed by strong FTs. According to the Figure 7 the mean magnetic field strength is strongly correlated to the strong FT area ratio. Unfortunately, we cannot state to what extent this is due to their number per area and to what extent to their size. Because it depends on both, with growing magnetic field strength, FTs grow in size but also their number might increase. Because of their unpredictable contribution (either with number or size) in the CH area there is no correlation between mean magnetic field strength and the area which goes along with the unpredictable evolutionary pattern as observed in the mean magnetic field strength.

### 6.3. Solar wind properties

In this study the corresponding HSS is observable in almost all solar rotations, from the beginning of a CH's lifetime up to its end. To a good extent it follows the area evolution for each CH individually. Which means that in the in-situ data we can expect slower or faster HSSs depending on the phase of the evolution of the CH from which it originates.

From previous studies we know that there exists a strong correlation between solar wind speed measured near Earth (L1 point) and area of their solar source, the CH (Krieger, Timothy, and Roelof, 1973; Nolte *et al.*, 1976; Vršnak, Temmer, and Veronig, 2007; Verbanac *et al.*, 2011; Rotter *et al.*, 2012, 2015; Hofmeister *et al.*, 2018; Heinemann *et al.*, 2018a). We checked the area-speed relation for our CHs with regular area evolution (CH1–CH6) for which we found no correlation. It only exists when considering each CH individually, but if we look at all of them together the scatter is to big. By correcting the CH area for its latitudinal dependence we find a lower scatter and an improvement in the correlation. With this we confirm that the HSS peak velocity is dependent on the co-latitude of their solar source and on the area (Hofmeister *et al.*, 2018). The scatter of speed is still relatively high, especially for smaller CH areas. That is expected since it is harder to precisely define a HSS the lower it's speed is. Another reason for the large scatter over all areas might be the high solar activity at the time of the observation. According to Tokumaru *et al.* (2017), in periods of solar maximum rapid structural changes in the corona and consequently in solar wind worsen the correlation between the two parameters.

The relation between CH area and the in-situ measured solar wind speed at 1AU persists over the entire evolution of a CH. This is important because it allows us to investigate the background processes in the CH during its entire lifetime. We derive a higher correlation coefficient for the growing than for the decaying phase considering regular CHs. This can be interpreted by different

physical mechanisms (still unknown) operating during the growing and decaying phase of a CH leading to different speeds of the solar wind.

## 7. Summary & Conclusion

On the basis of eight long-lived CHs that existed in the period from September 2010 until November 2015 we investigated the properties of the CH evolution. For this we analyzed and interpreted changes in morphology and magnetic properties as function of their evolution. The major findings are the classification of 6 out of 8 CHs as having a regular pattern of area evolution over time and with that the change of related parameters such as the open magnetic flux. They show two distinct phases, the growing and decaying phase. Since the magnetic field strength and FT flux ratio do not follow the evolutionary pattern of the area it is hard to argue when the CH is most stable. Although, observing changes in the magnetic flux and the HSS over time we can state that the CH is a rather stable structure in the solar atmosphere during the growing phase and around its maximum, enabling to generate a more stable HSS.

Since the research is done in the rising and maximum phase of the solar cycle, there are a lot of active regions in the vicinity of CHs. Active regions and in general eruptive events, support different processes which might cause abrupt changes in the observed CH area. Due to filament eruptions we have irregular area variations, as for CH7 and the last two points in CH4's evolution.

The dependence we found between the strong FTs area ratio and the mean magnetic field strength (Pearson $cc = 0.99$) shows that the mean magnetic field strongly depends on the area coverage of strong FTs. Moreover, the result that strong FTs consistently have a stronger influence on the total signed flux of a CH shows that strong FTs are dominating the evolution of magnetic properties of a CH. However, it might also work the other way around, that the growing magnetic field strength is influencing the growth of the strong FTs. We cannot state that their number is constant per area and the magnetic field depends on their number as well as on their size. That fact makes it harder to explain the magnetic field evolutionary pattern.

Clearly, the study showed that for a better understanding of CHs and their evolution we need to investigate into greater detail its fine structure in terms of magnetic elements. A key issue still open is the FT expansion as a function of height and how several multiple strong FTs, though spatially separated, generate the appearance of a continuous open structure. Other open questions are how those fine structure elements exactly change with time, and how the change of the CH position itself has influence on those elements and their evolution. Line-of-sight integrated intensities in the image data are a big drawback, however, combined modeling-observation efforts might shed more light on these outstanding issues.

**Acknowledgments** The *SDO* image data and the *ACE* in situ data is available by courtesy of NASA and the respective science teams. V.J. acknowledges support from University of Zagreb, Croatia, Erasmus+ program. S.G.H., M.T. and A.M.V. acknowledge funding by the

Austrian Space Applications Programme of the Austrian Research Promotion Agency FFG (859729, SWAMI). S.H. thanks the OEAD for supporting this research by a Mariett-Blau-fellowship. V.J. would like to thank the whole Graz group for all their support and for making this paper possible.

## Appendix

Table 2 gives detailed results on the Pearson correlation coefficients calculated for different parameters mentioned in the text. Figure 10 shows the change of the absolute value of flux balance (black) for CH1–CH6 together with the absolute value of the signed mean magnetic field strength (red) and area (dotted black) in time. Figure 11 shows the change of the unsigned (blue) and the absolute value of the signed (red) magnetic flux for CH1–CH6 together with the change of area in time (dotted black).

## References

Andreeva, O.A., Akhmetov, Z.S., Malashchuk, V.M., Zhigalkin, R.K.: 2018, Study of Variations of Some Characteristics of the Giant Coronal Hole of 2015-2017. *Geomagnetism and Aeronomy* **58**, 916. DOI. ADS.

Bilenko, I.A., Tavastsherna, K.S.: 2016, Coronal Hole and Solar Global Magnetic Field Evolution in 1976 - 2012. *Solar Phys.* **291**, 2329. DOI. ADS.

Bohlin, J.D.: 1977, Extreme-ultraviolet observations of coronal holes. I - Locations, sizes and evolution of coronal holes, June 1973-January 1974. *Solar Phys.* **51**, 377. DOI. ADS.

Bohlin, J.D., Sheeley, N.R. Jr.: 1978, Extreme ultraviolet observations of coronal holes. II - Association of holes with solar magnetic fields and a model for their formation during the solar cycle. *Solar Phys.* **56**, 125. DOI. ADS.

Couvidat, S., Schou, J., Hoeksema, J.T., Bogart, R.S., Bush, R.I., Duvall, T.L., Liu, Y., Norton, A.A., Scherrer, P.H.: 2016, Observables Processing for the Helioseismic and Magnetic Imager Instrument on the Solar Dynamics Observatory. *Solar Phys.* **291**, 1887. DOI. ADS.

Cranmer, S.R.: 2002, Coronal Holes and the High-Speed Solar Wind. *Space Sci. Rev.* **101**, 229. ADS.

Harvey, J.W., Sheeley, N.R.: 1978, Coronal holes, solar wind streams, and geomagnetic activity during the new sunspot cycle. *Solar Phys.* **59**(1), 159. DOI. ADS.

Heinemann, S.G., Temmer, M., Hofmeister, S.J., Veronig, A.M., Vennerstrøm, S.: 2018a, Three-phase Evolution of a Coronal Hole. I. $360^o$ Remote Sensing and In Situ Observations. *Astrophys. J.* **861**, 151. DOI. ADS.

Heinemann, S.G., Hofmeister, S.J., Veronig, A.M., Temmer, M.: 2018b, Three-phase Evolution of a Coronal Hole. II. The Magnetic Field. *Astrophys. J.* **863**, 29. DOI. ADS.

Heinemann, S.G., Temmer, M., Heinemann, N., Dissauer, K., Samara, E., Jerčić, V., Hofmeister, S.J., Veronig, A.M.: 2019, Coronal Hole Statistical Analysis and Catalogue covering the SDO-era. *arXiv e-prints*, arXiv:1907.01990. ADS.

Hiremath, K.M., Hegde, M.: 2013, Rotation Rates of Coronal Holes and their Probable Anchoring Depths. *Astrophys. J.* **763**, 137. DOI. ADS.

Hofmeister, S.J., Veronig, A., Reiss, M.A., Temmer, M., Vennerstrom, S., Vršnak, B., Heber, B.: 2017, Characteristics of Low-latitude Coronal Holes near the Maximum of Solar Cycle 24. *Astrophys. J.* **835**, 268. DOI. ADS.

Hofmeister, S.J., Veronig, A., Temmer, M., Vennerstrom, S., Heber, B., Vršnak, B.: 2018, The Dependence of the Peak Velocity of High-Speed Solar Wind Streams as Measured in the Ecliptic by ACE and the STEREO satellites on the Area and Co-latitude of Their Solar Source Coronal Holes. *Journal of Geophysical Research (Space Physics)* **123**, 1738. DOI. ADS.

Hofmeister, S.J., Utz, D., Heinemann, S.G., Veronig, A.M., Temmer, M.: 2019, The Magnetic Structure of Coronal Holes. *Astron. Astrophys.*. DOI.

**Table 2.** Pearson Correlation Coefficients Overview

| Relation | Fig. Nr. | $\mu$ | $\sigma$ | CI 90% | CI 95% | CI 99% |
|---|---|---|---|---|---|---|
| $\bar{B_s}$ vs. $\bar{B_{us}}$ CH1–CH6 | 4 | 0.83 | 0.05 | [0.75, 0.90] | [0.73, 0.92] | [0.68, 0.93] |
| $A_{CH}$ vs. $N_{FT}$ of strong FTs CH1–CH6 | 7 | 0.92 | 0.02 | [0.89, 0.95] | [0.88, 0.95] | [0.86, 0.96] |
| $A_{CH}$ vs. $N_{FT}$ of strong FTs growing phase | 7 | 0.94 | 0.02 | [0.91, 0.97] | [0.91, 0.97] | [0.89, 0.98] |
| $A_{CH}$ vs. $N_{FT}$ of strong FTs decaying phase | 7 | 0.87 | 0.05 | [0.80, 0.95] | [0.78, 0.96] | [0.74, 0.97] |
| $A_{CH}$ vs. $N_{FT}$ of weak FTs CH1–CH6 | 7 | 0.97 | 0.01 | [0.94, 0.98] | [0.93, 0.98] | [0.92, 0.99] |
| $A_{CH}$ vs. $N_{FT}$ of weak FTs growing | 7 | 0.98 | 0.01 | [0.96, 0.99] | [0.95, 0.99] | [0.93, 0.99] |
| $A_{CH}$ vs. $N_{FT}$ of weak FTs decaying | 7 | 0.95 | 0.02 | [0.92, 0.98] | [0.92, 0.99] | [0.90, 0.99] |
| $r_{A_{CH}}$ vs. $\lvert\bar{B_s}\rvert$ of strong FTs CH1–CH6 | 7 | 0.99 | 0.00 | [0.98, 0.99] | [0.98, 0.99] | [0.97, 1.00] |
| $r_{A_{CH}}$ vs. $\lvert\bar{B_s}\rvert$ of strong FTs growing phase | 7 | 0.99 | 0.01 | [0.98, 1.00] | [0.97, 1.00] | [0.97, 1.00] |
| $r_{A_{CH}}$ vs. $\lvert\bar{B_s}\rvert$ of strong FTs decaying phase | 7 | 0.98 | 0.01 | [0.96, 0.99] | [0.96, 0.99] | [0.95, 0.99] |
| $A_{CH}$ vs. $\lvert\bar{B_s}\rvert$ | 8 | 0.06 | 0.13 | [-0.14, 0.28] | [-0.17, 0.33] | [-0.23, 0.42] |
| $A_{CH}$ vs. $v_{HSS}$ CH1–CH6 | 9 | 0.26 | 0.19 | [-0.06, 0.57] | [-0.11, 0.60] | [-0.21, 0.66] |
| $A_{CH}$ vs. $v_{HSS}$ growing phase | 9 | 0.49 | 0.17 | [0.21, 0.77] | [0.16, 0.81] | [0.26, 0.90] |
| $A_{CH}$ vs. $v_{HSS}$ decaying phase | 9 | 0.26 | 0.22 | [-0.14, 0.58] | [-0.23, 0.62] | [-0.42, 0.71] |
| $A_{eff}$ vs. $v_{HSS}$ growing phase | 9 | 0.69 | 0.12 | [0.47, 0.87] | [0.41, 0.89] | [0.30, 0.92] |
| $A_{eff}$ vs. $v_{HSS}$ decaying phase | 9 | 0.45 | 0.14 | [0.20, 0.65] | [0.14, 0.68] | [-0.01, 0.74] |

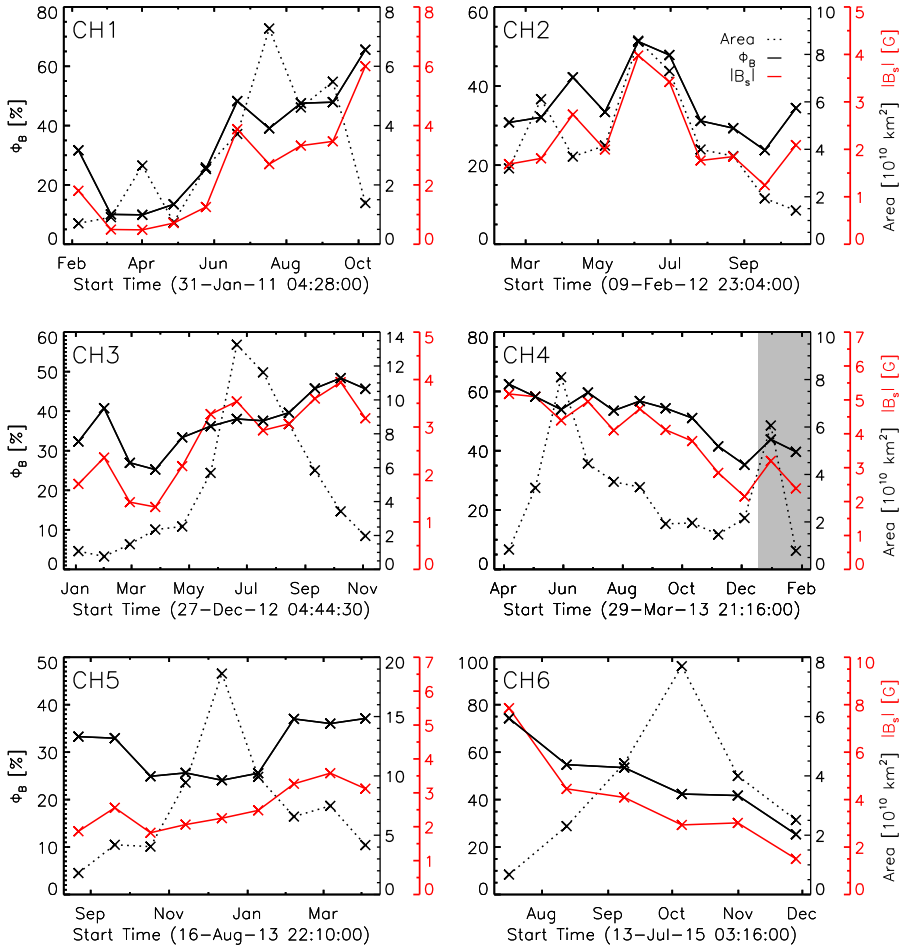


**Figure 10.** Evolution of the absolute value of the flux balance (black) plotted together with the absolute value of the signed mean magnetic field strength (red) and CH area (dotted black). The shaded area for CH4 marks the part of the evolution influenced by the filament eruption. Absolute value of the signed magnetic flux was plotted for easier visual representation.

Ikhsanov, R.N., Tavastsherna, K.S.: 2015, Latitude-temporal evolution of coronal holes in cycles 21-23. *Geomagnetism and Aeronomy* **55**, 877. DOI. ADS.

Jian, L., Russell, C.T., Luhmann, J.G., Skoug, R.M.: 2006, Properties of Stream Interactions at One AU During 1995 2004. *Solar Phys.* **239**, 337. DOI. ADS.

Krieger, A.S., Timothy, A.F., Roelof, E.C.: 1973, A Coronal Hole and Its Identification as the Source of a High Velocity Solar Wind Stream. *Solar Phys.* **29**, 505. DOI. ADS.

Lemen, J.R., Title, A.M., Akin, D.J., Boerner, P.F., Chou, C., Drake, J.F., Duncan, D.W., Edwards, C.G., Friedlaender, F.M., Heyman, G.F., Hurlburt, N.E., Katz, N.L., Kushner, G.D., Levay, M., Lindgren, R.W., Mathur, D.P., McFeaters, E.L., Mitchell, S., Rehse, R.A., Schrijver, C.J., Springer, L.A., Stern, R.A., Tarbell, T.D., Wuelser, J.-P., Wolfson, C.J., Yanari, C., Bookbinder, J.A., Cheimets, P.N., Caldwell, D., Deluca, E.E., Gates, R., Golub, L., Park, S., Podgorski, W.A., Bush, R.I., Scherrer, P.H., Gummin, M.A., Smith, P., Auker, G., Jerram, P., Pool, P., Soufli, R., Windt, D.L., Beardsley, S., Clapp, M., Lang, J., Waltham, N.: 2012, The Atmospheric Imaging Assembly (AIA) on the Solar Dynamics

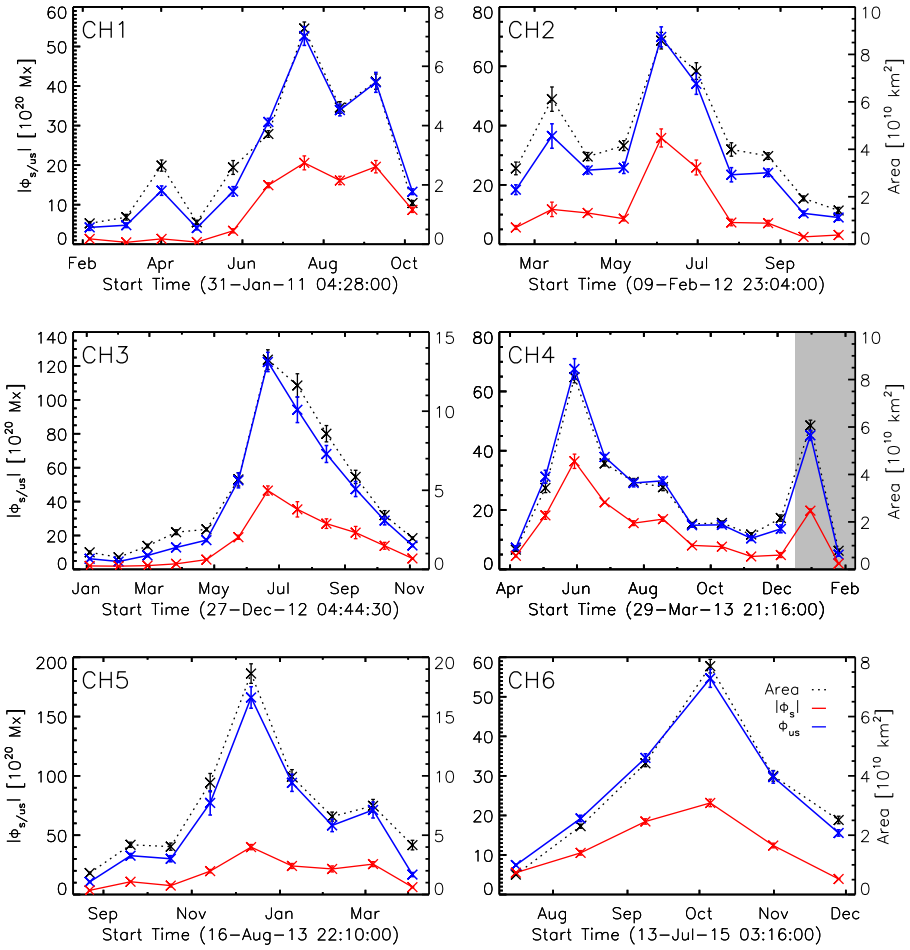


**Figure 11.** The signed (red) and unsigned (blue) magnetic flux for CH1–CH6 plotted together with the CH area (dotted black). The shaded area for CH4 marks the part of the evolution influenced by the filament eruption. Absolute value of the signed magnetic flux was plotted for easier visual representation.

Observatory (SDO). *Solar Phys.* **275**, 17. DOI. ADS.

McComas, D.J., Bame, S.J., Barker, P., Feldman, W.C., Phillips, J.L., Riley, P., Griffee, J.W.: 1998, Solar Wind Electron Proton Alpha Monitor (SWEPAM) for the Advanced Composition Explorer. *Space Sci. Rev.* **86**, 563. DOI. ADS.

Mikhailutsa, V.P.: 1995, The Dipole-Quadrupole Cycle of the Background Solar Magnetic Field. *Solar Phys.* **159**, 29. DOI. ADS.

Nolte, J.T., Krieger, A.S., Timothy, A.F., Gold, R.E., Roelof, E.C., Vaiana, G., Lazarus, A.J., Sullivan, J.D., McIntosh, P.S.: 1976, Coronal holes as sources of solar wind. *Solar Phys.* **46**, 303. DOI. ADS.

Pesnell, W.D., Thompson, B.J., Chamberlin, P.C.: 2012, The Solar Dynamics Observatory (SDO). *Solar Phys.* **275**, 3. DOI. ADS.

Richardson, I.G., Cane, H.V.: 2010, Near-Earth Interplanetary Coronal Mass Ejections During Solar Cycle 23 (1996 - 2009): Catalog and Summary of Properties. *Solar Phys.* **264**, 189. DOI. ADS.

Rotter, T., Veronig, A.M., Temmer, M., Vršnak, B.: 2012, Relation Between Coronal Hole Areas on the Sun and the Solar Wind Parameters at 1 AU. *Solar Phys.* **281**, 793. DOI. ADS.

Rotter, T., Veronig, A.M., Temmer, M., Vršnak, B.: 2015, Real-Time Solar Wind Prediction Based on SDO/AIA Coronal Hole Data. *Solar Phys.* **290**, 1355. DOI. ADS.

Schou, J., Scherrer, P.H., Bush, R.I., Wachter, R., Couvidat, S., Rabello-Soares, M.C., Bogart, R.S., Hoeksema, J.T., Liu, Y., Duvall, T.L., Akin, D.J., Allard, B.A., Miles, J.W., Rairden, R., Shine, R.A., Tarbell, T.D., Title, A.M., Wolfson, C.J., Elmore, D.F., Norton, A.A., Tomczyk, S.: 2012, Design and Ground Calibration of the Helioseismic and Magnetic Imager (HMI) Instrument on the Solar Dynamics Observatory (SDO). *Solar Phys.* **275**, 229. DOI. ADS.

Stone, E.C., Cohen, C.M.S., Cook, W.R., Cummings, A.C., Gauld, B., Kecman, B., Leske, R.A., Mewaldt, R.A., Thayer, M.R., Dougherty, B.L., Grumm, R.L., Milliken, B.D., Radocinski, R.G., Wiedenbeck, M.E., Christian, E.R., Shuman, S., von Rosenvinge, T.T.: 1998, The Solar Isotope Spectrometer for the Advanced Composition Explorer. *Space Sci. Rev.* **86**, 357. DOI. ADS.

Temmer, M., Hinterreiter, J., Reiss, M.A.: 2018, Coronal hole evolution from multi-viewpoint data as input for a STEREO solar wind speed persistence model. *Journal of Space Weather and Space Climate* **8**, A18. DOI. ADS.

Tokumaru, M., Satonaka, D., Fujiki, K., Hayashi, K., Hakamada, K.: 2017, Relation Between Coronal Hole Areas and Solar Wind Speeds Derived from Interplanetary Scintillation Measurements. *Solar Phys.* **292**, 41. DOI. ADS.

Tsurutani, B.T., Gonzalez, W.D., Gonzalez, A.L.C., Guarnieri, F.L., Gopalswamy, N., Grande, M., Kamide, Y., Kasahara, Y., Lu, G., Mann, I., McPherron, R., Soraas, F., Vasyliunas, V.: 2006, Corotating solar wind streams and recurrent geomagnetic activity: A review. *Journal of Geophysical Research (Space Physics)* **111**, A07S01. DOI. ADS.

Verbanac, G., Vršnak, B., Veronig, A., Temmer, M.: 2011, Equatorial coronal holes, solar wind high-speed streams, and their geoeffectiveness. *Astron. Astrophys.* **526**, A20. DOI. ADS.

Verbanac, G., Živković, S., Vršnak, B., Bandić, M., Hojsak, T.: 2013, Comparison of geoeffectiveness of coronal mass ejections and corotating interaction regions. *Astron. Astrophys.* **558**, A85. DOI. ADS.

Vršnak, B., Temmer, M., Veronig, A.M.: 2007, Coronal Holes and Solar Wind High-Speed Streams: I. Forecasting the Solar Wind Parameters. *Solar Phys.* **240**, 315. DOI. ADS.

Webb, D.F., Nolte, J.T., Solodyna, C.V., McIntosh, P.S.: 1978, Evidence linking coronal transients to the evolution of coronal holes. *Solar Phys.* **58**, 389. DOI. ADS.

Wilcox, J.M.: 1968, The Interplanetary Magnetic Field. Solar Origin and Terrestrial Effects. *Space Sci. Rev.* **8**, 258. DOI. ADS.